Near-Edge X-ray Absorption Fine Structure Investigations of Order in Carbon Nanotube-Based Systems†

Sarbajit Banerjee,[‡,§] Tirandai Hemraj-Benny,[§] Sharadha Sambasivan,[||] Daniel A. Fischer,[||] James A. Misewich,[⊥] and Stanislaus S. Wong*[,§,⊥]

Department of Chemistry, State University of New York at Stony Brook, Stony Brook, New York 11794-3400, Materials Science and Engineering Laboratory, National Institute of Standards and Technology, Gaithersburg, Maryland 20899, and Materials Sciences Department, Brookhaven National Laboratory, Bldg. 480, Upton, New York 11973

Received: June 15, 2004; In Final Form: October 24, 2004

Probing order in nanotube systems is of fundamental importance in devising applications of these tubes in field emission applications as well as for components of composite materials. We use near-edge X-ray absorption fine structure (NEXAFS) spectroscopy to qualitatively and quantitatively study the degree of order and alignment in a wide range of carbon nanotube-based systems, including single-walled carbon nanotube (SWNT) powder, SWNT films, and aligned multiwalled carbon nanotubes. The results are compared to analogous data obtained from a highly ordered pyrolytic graphite (HOPG) sample.

Introduction

Carbon nanotubes have attracted tremendous interest due to their interesting fundamental properties, as well as for their promise in applications such as in molecular electronics, structural materials, field emitters, actuators, capacitors, components of composites, and in gas storage, to name just a few of the possibilities that have been explored.[1−4] Although the applicability of single carbon nanotube devices has been extensively studied, it is likely that many functional nanoscale materials will require the controllable incorporation of multiple carbon nanotubes into arrays. In these spatial configurations, it is likely that the advantageous anisotropic properties of these nanotubes will be more readily exploitable as compared with bulk samples. In bulk, these properties are likely to be orientationally averaged out, due to the presence of bundles of tubes that are entangled and disordered. For example, the use of carbon nanotubes as field emitters in flat panel displays requires them to be patterned into aligned arrays or films.[4,5] Similarly, the mechanical properties of composite materials for high-strength applications are optimized by increasing the ordering of nanotubes in fibers or films.[6−8]

A number of different approaches toward fabricating ordered nanotube systems have been developed. These include growth of nanotubes on patterned catalyst arrays,[9−11] chemical vapor deposition and related aerosol pyrolysis methods,[12,13] postsynthetic treatments to generate films and fibers,[6,8,14] as well as lithographically inspired techniques.[15,16] However, characterization of order and alignment in these arrays is not straightforward.

Polarization Raman spectroscopy has been used to investigate order in fibers and forests of single walled carbon nanotubes (SWNTs).[14,17] However, Raman spectroscopy is very sensitive to the electronic structure of SWNTs,[18] and thus, Raman intensities can be greatly affected by factors such as charge transfer, surface modification, degree of aggregation in bundles, and strain.[19−21] This limits the applicability of polarization Raman spectroscopy in studying order in nanotube-based composite materials. Polarized absorption spectroscopy of aligned nanotube fibers and composites show that the optical transitions between the van Hove singularities in SWNTs are strongly polarized along the nanotube axis.[22] In addition, X-ray scattering has been utilized to characterize ordering in nanotube fibers in a complementary fashion.[23]

NEXAFS as a Tool for Probing Aligned Nanotubes. Herein, we present near-edge X-ray absorption fine structure (NEXAFS) spectroscopy as a technique for studying order and alignment in nanotube arrays and composites. NEXAFS spectroscopy involves the excitation of electrons from a core level to partially filled and empty states. The peak positions and spectral line shape in a NEXAFS spectrum are directly related to the nature of these unoccupied electronic states. More specifically, in the context of carbon-based structures such as carbon nanotubes, NEXAFS measurements can detect specific bonds in molecules (e.g., C═C, C−C, and C−O bonds) as well as angular dependence of the specific orbitals involved.[22] Moreover, though the position of the σ resonance is a measure of the intramolecular bond length, the location and intensity of the lower energy π^* resonance can provide insights into bond hybridization. The transitions, i.e., 1s $\rightarrow \pi^*$ and 1s $\rightarrow \sigma^*$, can be thought of as dipole transitions from initial *s* states to the *p* component of the π^* and σ^* final states, respectively. The transition matrix elements thus have an angular dependence on the angle made by, for instance, the π^* orbital with respect to the electric field vector of the incident polarized X-rays.[24] Because the light from the synchrotron source used is linearly polarized, the intensity of the σ^* and π^* transitions will be sensitive to the orientation of these orbitals with respect to the polarization vector. Thus, changes in the intensity of resonances

† Part of the special issue "George W. Flynn Festschrift".

* To whom correspondence should be addressed. E-mail: sswong@notes.cc.sunysb.edu; sswong@bnl.gov.

‡ Current address: Department of Applied Physics and Applied Mathematics, Columbia University, New York, NY 10027.

§ State University of New York at Stony Brook.

|| National Institute of Standards and Technology.

⊥ Brookhaven National Laboratory.

10.1021/jp047408t CCC: $30.25
Published on Web 02/08/2005

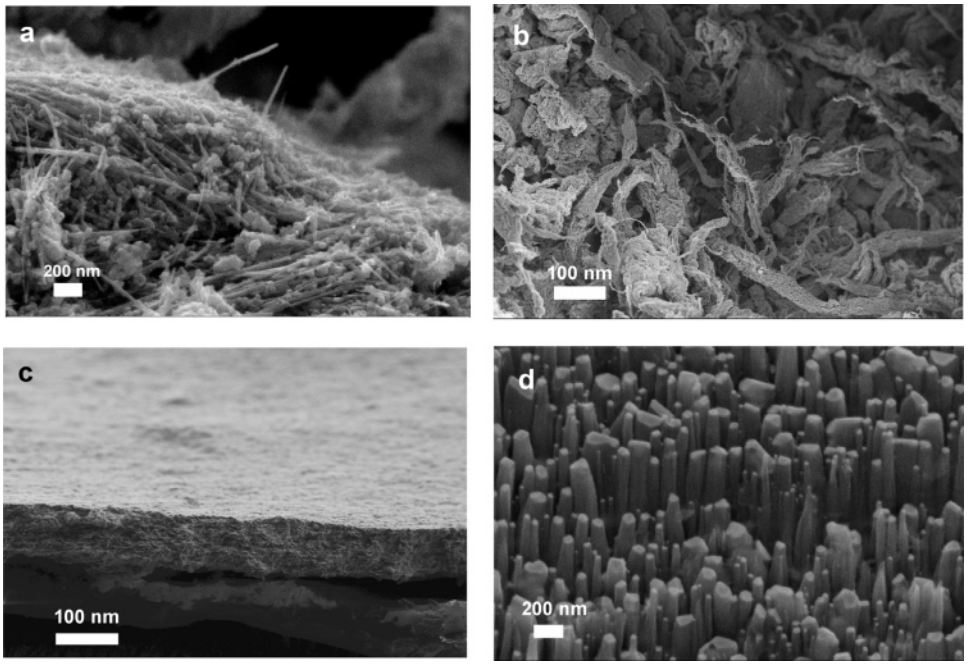

Figure 1. SEM images of (a) raw MWNT powder, (b) raw SWNT HiPco powder, (c) tilt view of SWNT buckypaper, and (d) aligned MWNTs grown on Pt substrates.

upon rotating the sample in the plane of incidence of the beam provide evidence for bond orientation.

In previous work, NEXAFS has been used to measure varying degrees of bond hybridization in mixed sp^2/sp^3 bonded carbon materials, the presence of defects in nanotubes, amorphous precursors to multiwalled carbon nanotubes, and the nature of oxygen-containing functional groups on carbon nanotubes.[25−29] We recently demonstrated the application of NEXAFS spectroscopy in probing the degree of covalent sidewall functionalization in ozonized SWNTs.[29]

As precedence for the current work, studies of the angular dependence of the π^* resonance have been performed of multiwalled nanotube (MWNT) powders, grown by chemical vapor deposition.[26] No systematic change of the intensity of this peak was observed with variation in the polarization angle, indicating that the nanotubes in the specimen were randomly distributed with no preferred orientation. It was also predicted that "specially grown tubes with preferred orientation" might exhibit an angular dependence of the π^* resonance.[26] Peaks in the valence photoelectron spectra of macroscopically aligned MWNTs have been previously compared with calculations for graphite; in the same work, nanotube orientation was determined using C 1s X-ray absorption spectroscopy measurements, including an evaluation of the π^* and σ^* intensities as a function of light incidence angle and tube orientation.[30] Another recent angle-dependent XANES study of arrays of MWNTs reported an enhancement of both π^* and σ^* C K-edge intensities at the tips of carbon nanotubes.[31]

In the current manuscript, we observe an angular dependence in "buckypaper" or SWNT films, where the nanotubes are confined to a single plane, as well as in arrays of MWNTs grown on Pt substrates. We compare our results to those of randomly oriented tubes in SWNT and MWNT powders, confirming the effects of angular anisotropy in data interpretation.

It is noteworthy that we did not observe a tip enhancement for our oriented MWNT samples.[31] Such an effect was also not noted in studies of dense arrays of oriented SWNT and MWNTs, that will be reported in a subsequent publication. We explain our observations as arising from physical differences in tip morphology between literature samples vs our own samples (which were prepared by dissimilar means) as well as discrepancies in the actual area of the arrays that was being probed (which was determined by the bias voltage).

Experimental Section

Sample Preparation. *HOPG.* A block of highly ordered pyrolytic graphite (Grade ZYA) was purchased from Advanced Ceramics Corp. and was freshly cleaved before measurement.

SWNTs. Tubes, synthesized using the high pressure CO decomposition (HiPco) method, were purchased from Carbon Nanotechnologies Inc., and were subsequently processed to make free-standing films, known as "buckypaper". Specifically, HiPco SWNTs were treated with a 30% H_2O_2 solution to remove some of the amorphous carbon content.[32] The resulting suspension was filtered over a 0.2 μm polycarbonate membrane to generate a free-standing, compacted film of SWNTs. After washing with water, the film was dried in an oven at 100 °C overnight. The properties of SWNT buckypaper have been reviewed recently.[6] These films consist of SWNTs, aligned within the *xy*-plane of the membrane, but otherwise randomly oriented. SEM images of samples are presented in Figure 1b,c.

MWNTs. Aligned MWNT arrays, grown by chemical vapor deposition on Pt surfaces,[11] were obtained from NanoLab (Newton, MA) and have densities of 10^8-10^9 nanotubes/cm^2. The nanotubes range from 50 to 150 nm in outer diameter and are 10 μm in length. MWNTs grown on arrays have been compared with powders of MWNTs (>95% purity, Nanolab) in this experiment to compare their relative anisotropies. SEM images are presented in Figure 1a,d.

NEXAFS Measurements. C K-edge NEXAFS spectra were taken at the U7A NIST/DOW end station at the National Synchrotron Light Source (NSLS) at Brookhaven National Laboratory. The partial electron yield (PEY) signal was collected using a channeltron electron multiplier with an adjustable entrance grid bias (EGB). A negative bias of 50 V was applied for the current set of data to prevent low-energy photoelectrons from reaching the detector. A monochromator with a 600 line/

mm grating, providing for ~0.15 eV resolution, was used for all of the NEXAFS spectra collected. In addition, the spectra were collected at different polarization angles by rotating the sample holder with respect to the incident beam in the plane of incidence. The monochromator energy scale was calibrated using the carbon K-edge π^* transition of graphite, located at 285.35 eV. For the actual data collection, the powder samples were smeared onto a Cu tape and mounted onto a sample bar inside a UHV chamber. Pieces of buckypaper were cut and mounted onto Cu tape. In particular, to eliminate the effect of incident beam intensity fluctuations and monochromator absorption features, the PEY signals were normalized using the incident beam intensity obtained from the photoemission yield of a clean Au grid with 90% transmittance.

The edge jump for the C K-edge is defined as the intensity difference at energies before the onset of C K-edge measurements (e.g., <280 eV) and after the transitions (e.g., >320 eV). These spectra have been processed through standard pre- and post-edge normalization routines. The pre-edge was subtracted to zero followed by post-edge-jump normalization performed by dividing the pre-edge-jump normalized spectra by the edge jump intensity obtained far above the K-edge, beyond 320 eV. This results in an edge jump of unity. Thus, changes in spectral intensity observed arise from anisotropy in the system and are independent of total carbon content. A comparison of intensities at different polarization angles is made by subtracting an arctangent function to account for the C K-edge jump and thereafter by fitting the π^* and σ^* resonances to a Gaussian.

Results

Figure 2a shows the changes in NEXAFS partial electron yield (PEY) intensities at different incident angles for HOPG graphite. The first π^* resonance occurs at approximately 285 eV; broad σ^* resonances occur in the region from 290 to 315 eV. HOPG graphite is an ideal system. The π^* orbitals are aligned normal to the surface, whereas the σ^* plane is localized along the surface (inset to Figure 2a). Thus, at normal incidence (90°), the electric field vector is parallel to the surface and normal to the π^* orbitals. At glancing incidence (20°), the electric field vector has a large projection onto the π^* orbitals and thus, the intensity of the π^* resonance is at a maximum.[24] A plot of the π^* intensity vs the incidence angle shows a classic cosine-squared dependence as shown in Figure 2b.

Conversely, the intensity of the σ^* bound exciton[33] at ~292.1 eV shows the reverse behavioral dependence. At normal incidence, the electric field vector is in the plane of the σ^* orbitals, and thus, at this angle, the σ^* resonance is at its maximum. At glancing incidence, the electric field vector is out of the plane, and has only a small projection in the plane. Thus, the intensity of this resonance is highly attenuated. The intensity of the σ^* resonance has a sine-squared dependence with respect to the incidence angle as shown in Figure 2c.

NEXAFS spectra of both MWNTs and SWNTs are quite similar to those of graphite.[29,34] The spectra are characterized by a sharp C—C π^* transition near 285.4 eV, a sharp σ^* bound exciton near 292 eV, two other σ^* transitions from 292 to 298 eV, and broad ($\sigma + \pi$) transitions from 301 to 309 eV.[29] Two small peaks also occur in the 287—290 eV region that can be assigned to oxygenated surface functionalities introduced while the tubes are processed.[28,29] These correspond to π^* C═O and σ^* C—O resonances.

Figure 3 shows the variation in intensity with incidence angle for the π^* resonance in SWNT buckypaper. It is apparent that the bucky paper shows the same trend as with HOPG graphite,

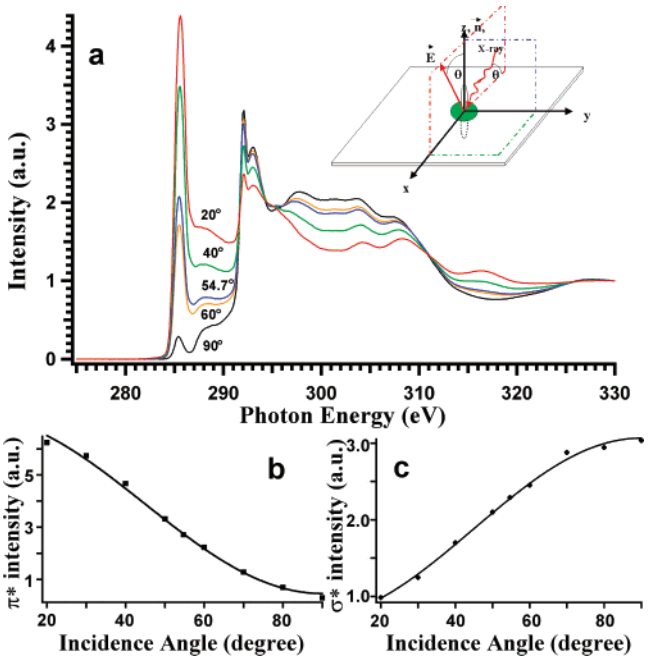

Figure 2. (a) C K-edge PEY spectra of freshly cleaved HOPG graphite taken at retarding potentials of −50 V, after rotating the sample in the plane of incidence (intervals from 20° to 90°) to the incident beam. Selected spectra are shown. All the spectra have been pre and postedge normalized. Inset shows the geometry of π^* vector orbitals and σ^* planes with respect to the incident beam and the electric field vector, **E**, which remains perpendicular to the incident X-ray irradiation. (b) Integrated intensity of π^* resonance at different angles of incidence. Solid line is a fit to the cosine function used to determine b/a values of normalized amplitude. Further details are included in the text. (c) Integrated intensity of the σ^* bound exciton resonance at different angles of incidence. (Solid line is a fit to a sine-squared function. Intensities of π^* and σ^* resonances were determined by subtracting an arctan function from the pre- and postedge normalized spectra to simulate the edge jump, followed by fitting of the π^* or σ^* peaks with a Gaussian.) Errors in integrated areas are ± 1.5%.

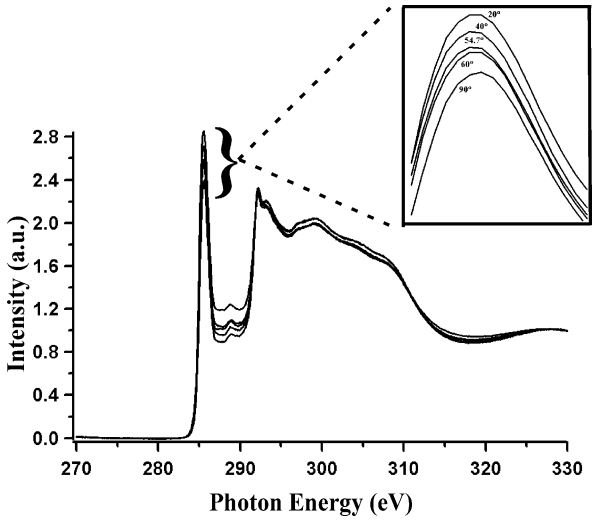

Figure 3. C K-edge spectra of SWNT buckypaper taken at retarding potentials of −50 V after rotating the sample in the plane of incidence (intervals from 20° to 90°) to the incident beam. Selected spectra are shown. All the spectra are pre- and postedge normalized. Inset shows an expanded π^* region. From top to bottom, data corresponding to angles of incidence of 20°, 40°, 54.7°, 60°, and 90°, respectively, are shown.

namely an inverse dependence of the π^* intensity with increasing incidence angle. However, it is also evident that in this case,

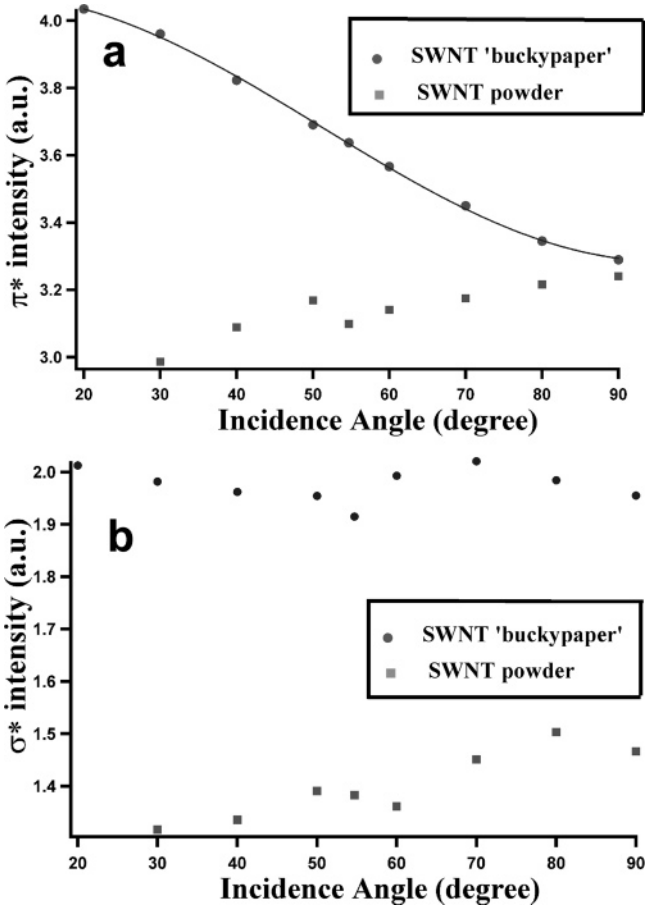

Figure 4. (a). Integrated intensity of π^* resonances at different angles of incidence. Circles correspond to the SWNT buckypaper, and squares correspond to SWNT powder. Solid line is a fit to the cosine function used to determine (b/a) values of normalized amplitude. Further details are described in the text. (b). Integrated intensity of the σ^* bound exciton resonance at different angles of incidence. Circles correspond to the SWNT buckypaper, and squares correspond to the SWNT powder sample. Errors in integrated areas are ±1.5%.

the trend is not as pronounced as that of HOPG graphite. In other words, the nanotube sample shows far less anisotropy than HOPG graphite though there is still some angular dependence of the π^* intensity. In subsequent sections, we analyze similarities and differences between HOPG graphite and SWNT buckypaper that can account for the varied angular dependences of their π^* intensities.

For the σ^* resonances, there does not appear to be a systematic variation in intensity with incidence angle. Due to the uncertainty in determining the precise location of the edge jump as well as overlap from mixed ($\sigma + \pi$) states, the peak areas of σ^* peaks could not be unambiguously ascertained. It is well known though that there is significant π^* mixing in orbitals, which is further enhanced in nanotubes due to curvature-induced rehybridization effects. This is apparent in the relative broadening of the so-called bound exciton peak in nanotubes as compared with graphite. Thus, in this work, we focus primarily on the π^* peak.

The anisotropy observed in the behavior of π^* resonances arises primarily from having spatially constrained SWNTs within the *xy*-plane of the paper. This is apparent by comparison with the analogous data for SWNT powders, where there is no order in either the π^* or σ^* resonances. Figure 4 depicts the variation in intensity of the π^* and σ^* resonances with angle of incidence in the buckypaper and in the powder. The random orientation of tubes in the powder accounts for the lack of any angular polarization trend observed with either the π^* or the σ^* resonances.

Discussion

To understand these results, we proceed to evaluate the angular dependencies that would be expected for different orientations of tubes. Figure 5 shows three possible orientations of nanotubes on a surface. In a buckypaper or a SWNT film, nanotubes would be constrained to lie within the *xy*-plane of the paper. That is, the vast majority of tubes would have orientations depicted by tube A (tube lying along *x*-axis), tube B (tube lying along *y*-axis), and all conceivable intermediate positions between them in the *xy*-plane. Thus, in a given buckypaper sample, a random mixture of A, B, and intermediate positions may be expected. In aligned SWNT fibers, all the tubes should point in a specific direction. On the other hand, in arrays or forests of nanotubes, the tubes are expected to point upward, as shown with tube C (tube lying along *z*-axis). Herein, we discuss the polarization dependence expected individually for the three model tubes.

In a flat HOPG graphite substrate (Figure 2a, inset), as the angle of incidence changes from glancing to normal, the direction of the resultant electric field vector (**E**) changes in the *xz* plane as shown, and always remains perpendicular to the direction of propagation of the incident beam. When the electric field vector is aligned at 90° to the surface, the π^* resonance has the maximum intensity. At normal incidence, when the electric field vector is at 0° to the surface, the field is perpendicular to the π^* orbital and thus has no component along that direction.

For tube A, at normal incidence, the electric field vector runs along the tube axis and therefore is orthogonal to the π^* orbitals, which stick out of the tubes like spokes and lie in the *yz* plane (Figure 5ii). At glancing incidence, however, **E** has a large projection onto the same plane as the π^* orbitals (the *yz* plane). Thus, the π^* resonance intensity will be the highest at glancing incidence. Thus, in general, tube A will follow the same trends as HOPG graphite. However, for the same number of carbon atoms, the HOPG sheet will have a higher π^* intensity because in the cylindrical tube, **E** will have different inequivalent projections onto different π^* orbitals. This is clear in Figure 5ii where the π^* orbital labeled **4**, for instance, is perpendicular to **E** even at glancing incidence, and thus will not contribute to the π^* intensity. In contrast, the other three orbitals, **1**−**3**, contribute to different extents at each incidence angle, depending on the projections made by **E** onto each individual orbital. Thus, it is clear that the anisotropy spread at different incident angles is intrinsically much less for nanotubes than for graphite. The expected angular dependence for tube A is shown in Figure 6 (dotted line) and is calculated using a graphite-like dependence from Figure 2b.

Tube B shows an entirely different angular dependence. As depicted in Figure 5iii, at normal or glancing incidence, the electric field vector has exactly the same sum projections onto the π^* orbitals. In other words, **E** rotates in the same *xz* plane as that of the π^* orbitals, and always experiences an identical field environment. This tube thus exhibits completely isotropic behavior, which would be seen as a straight line in a plot of normalized intensity vs angle. This is seen in Figure 6 (dashes and dots). It is important to note that tube B does not merely experience the mirror trend from that of tube A. The field is simply isotropic at all angles. Thus, if both tubes A and B are present in a sample, the result would be remnant anisotropy

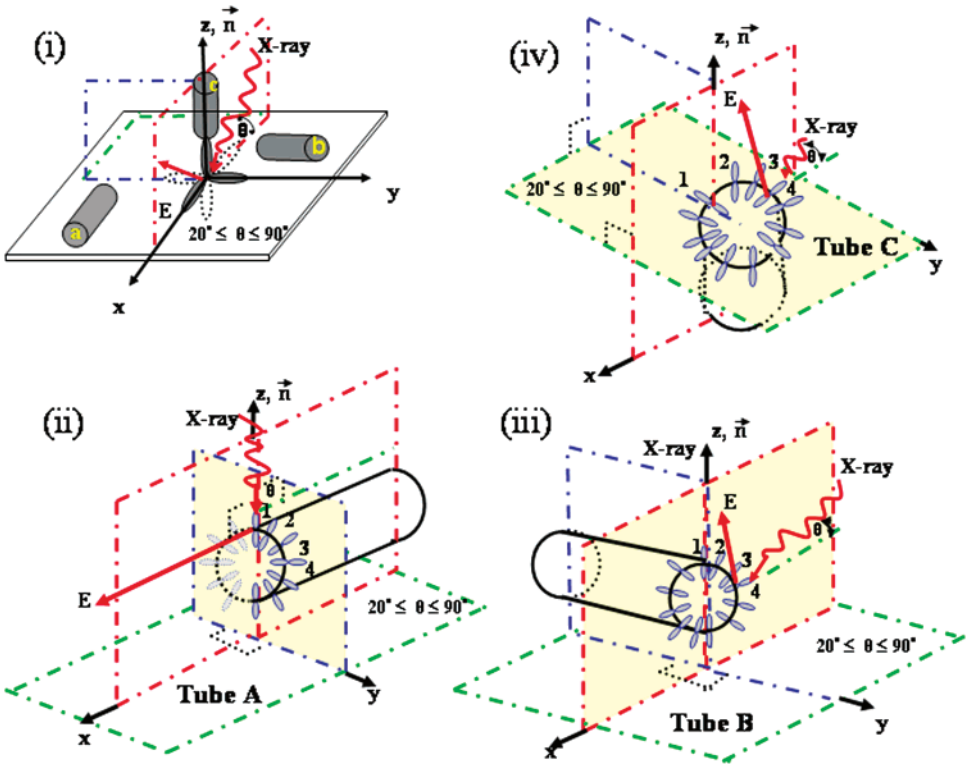

Figure 5. (i). Schematic depiction of three possible orientations of nanotubes aligned along Cartesian axes: tube A (along *x*-axis), tube B (along *y*-axis), and tube C (along *z*-axis). The π^* orbitals are in the *yz*, *xz*, and *xy* planes, respectively. (ii), (iii), and (iv) show the orientations of π^* orbitals for each of the different nanotubes with respect to the electric field vector and the incident beam. The angle of incidence changes from glancing (20°) to normal (90°) with the electric field vector always in a perpendicular orientation to the direction of propagation. The incident beam always rotates in the *xz* plane. Please see text for further details.

due to tube A, but there would be a reasonable π^* signal even at normal incidence. Thus, a mixture of tubes oriented in the *x* and *y* directions will show anisotropy to a lesser degree, due to a smearing out of order by tubes oriented similarly to tube B, thereby adding an intercept to a plot of intensity vs angle. Any tube intermediate to the boundary conditions represented by tubes A and B will show the same qualitative trend as the vectorial summation of A and B, i.e., the presence of remnant anisotropy, the extent of which will depend on the precise orientation of the tube within the plane. Thus, it must be noted that films will intrinsically have much lower anisotropy than graphite. In other words, the SWNT buckypaper cannot be expected to show the exact same behavior as HOPG graphite both due to intrinsic curvature effects as well as due to disorder within the plane of the buckypaper.

Tube C, however, clearly shows the reverse trend from that of tube A (Figure 5iv). Indeed, for tube C, which stands upright, at normal incidence, **E** is in the same *xy* plane as the π^* orbitals, and thus, the π^* resonances will be the highest at this angle, as opposed to at glancing angles (Figure 5iv). Conversely, when **E** is normal to the surface, the field lies along the tube axis (along *z*) and is perpendicular to the plane of the π^* orbitals. Thus, tube C will experience the reverse trend to that noted with HOPG graphite and with tube A. Specifically, there is an increase in the intensity of the π^* resonance with increasing angle of incidence. This is seen in Figure 6 (dashed line), which shows the opposite trend to that of tube A (dotted line). Similar geometric arguments have been presented previously.[30]

In samples of SWNT and MWNT powder, the presence of upright tubes (with axes along the *z*-axis, tube C-like species), clearly showing the reverse behavior of tube A, leads to randomness and angular isotropy by canceling out any angular dependence of tubes oriented along the *x*-axis (tube A-like species). This observation has been reported previously by a different group.[26]

In the SWNT buckypaper specimen, the beam samples thousands of randomly oriented nanotubes. The remnant HOPG-like anisotropy observed for the π^* resonances (Figure 4a) in buckypaper indicates that there is not a sufficient quantity of upright tubes, exhibiting tube C-like behavior to completely cancel out projections along the *x*-axis (tube A-like species). This suggests that the tubes have been constrained to lie in the plane of the buckypaper, thereby introducing detectable anisotropy in the sample. The presence of tube B-like species is thus the reason for the lower degree of anisotropy as compared to HOPG graphite as seen in Figures 2b and 4a. That is, the behavior observed can be attributed to a vectorial combination of tube A and tube B-like species, explaining the anisotropy observed in Figures 2b and 4a.

To evaluate this more quantitatively, we fitted the experimental plot of integrated π^* intensities for the bucky paper to a weighted sum of the functions used for the angular dependencies of tubes A, B, and C, as shown by the solid line in Figure 6. This serves as a good estimate of the relative contribution of different species to the buckypaper π^* intensities. Upon deconvolution, we see that only about 13% of the tubes have a tube C-like orientation. The vast majority, ~87%, of tubes is constrained to lie in the plane. tube A-like species and tube B-like species contribute about ~31% and 56%, respectively, to the weighted sum depicted by the solid line. The anisotropy observed in the experimental data correlate well with the relatively low anisotropy expected for these structures, as discussed above. This further demonstrates the sensitivity of NEXAFS in determining order in these systems.

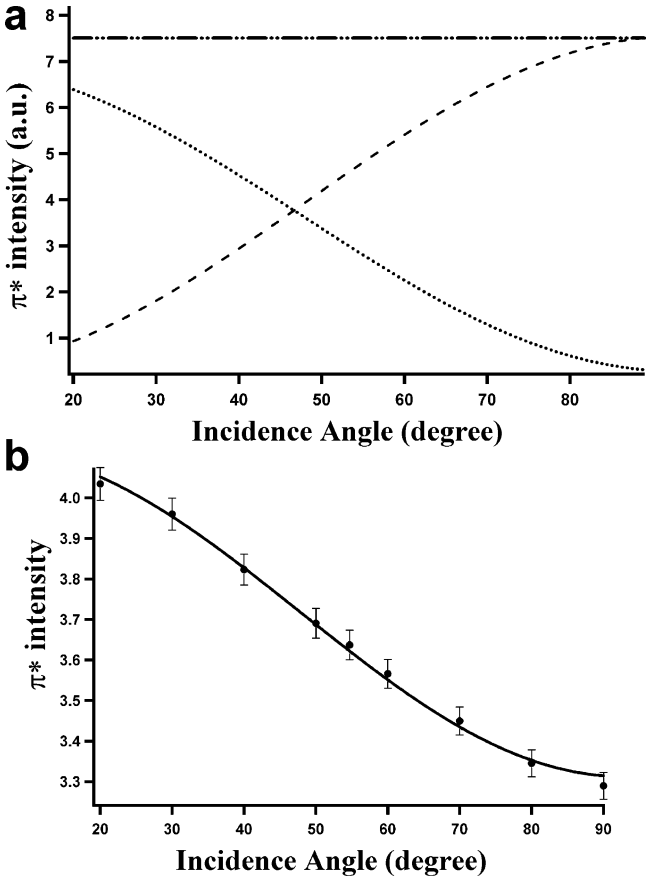

Figure 6. Calculating the proportion of tubes constrained to lie in the plane. (a). Dotted line (···) represents the predicted anisotropy for a sample with all the tubes aligned in the direction of tube A. The dash/dotted line combination (-•-•-•-) shows the predicted anisotropy for a sample with all the tubes aligned in the direction of tube B. Dashed line (- - -) depicts the predicted anisotropy for a sample with all the tubes aligned in the direction of tube C. (b). Filled circles are integrated π^* intensities for the SWNT buckypaper at different angles of incidence. Solid line is the weighted sum of the contributions of tube A (~31%), tube B (~56%), and tube C (~13%), which have been fitted to the experimental trend noted for the buckypaper mat.

Evaluation of Order in Nanotube Systems. To quantify the degree of alignment in the bucky papers, we use two different order parameters. The first involves fitting the intensity vs angle plot for π^* resonances in Figure 4a to a cosine function.[35]

$$I(\theta) = a + b\cos(2(\theta - \gamma)) \quad (1)$$

The normalized amplitude defined as (b/a) has been shown to be related to the order parameter of the transitional dipole moment.[35] For a three-dimensional, randomly oriented sample, this value of the normalized amplitude should be close to 0, whereas for an ordered sample with all the π^* orbitals perpendicular to the surface, the order parameter should be 1. Indeed, in Figure 2b, we show the fit of eq 1 to data for HOPG graphite. The normalized amplitude (b/a) was determined to be 0.921, indicating almost perfect order. Figure 4a shows the fit for the SWNT buckypaper. The normalized amplitude was calculated to be 0.0904, indicating much less sample anisotropy than graphite. However, in comparison with previous literature on polymer chains, a value of ~0.1 still shows substantial alignment in the sample.[35] As discussed above, our data are not surprising, because the spread of anisotropy in nanotube films is predicted to be much less than in HOPG through the simple curvature and azimuthal disorder arguments presented above. No meaningful fit could be obtained for the π^* data of the SWNT powder sample.

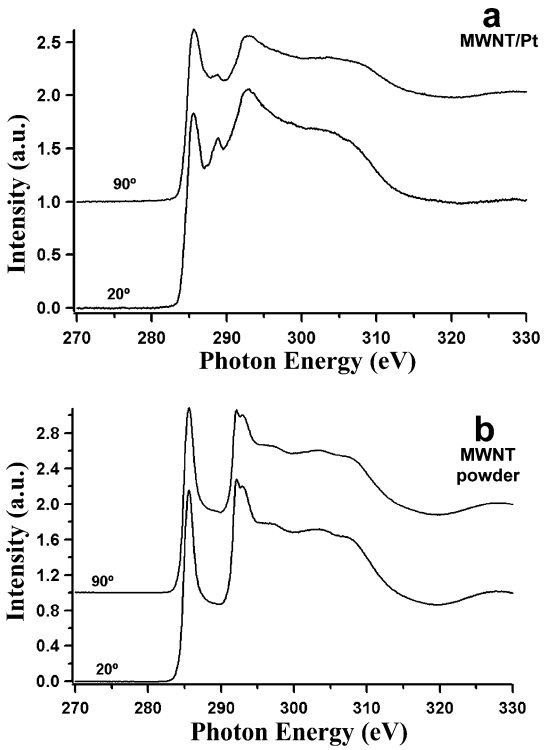

Figure 7. C K-edge spectra of (a) MWNTs grown on Pt and (b) MWNT powder taken at retarding potentials of −50 V after rotating the samples in the plane of incidence. Top spectra are at normal (90°) incidence and bottom spectra are at glancing (20°) incidence in each case. All the spectra have been pre- and postedge normalized.

A second, further orientation parameter (OP) is defined as

$$\mathrm{OP} = (I_\perp - I_{||})/(I_\perp + I_{||})^{36} \quad (2)$$

where I is the intensity at normal incidence and $I_{||}$ is the intensity at grazing incidence. Values close to 1 indicate higher order. The OP for HOPG graphite is −0.902, with the negative sign indicating that the π^* resonance decreases in intensity with increasing angle of incidence. It is instructive to compare orientation parameters for SWNT bucky paper and powder. The bucky paper has an OP value of −0.0933, whereas the SWNT powder has an OP of 0.0407, opposite in sign to that of HOPG graphite. Thus, constraining SWNTs in two dimensions causes tubes to show the sample anisotropy as discussed above. From the definition of the order parameters described above, remnant intensity at normal incidence, arising from the presence of tube B-like species, will result in more disorder and consequently, a smaller order parameter than that seen in graphite. These order parameters can be used to compare ordering and alignment in films of nanotubes prepared by different methods.[6]

MWNT Arrays on a Pt Substrate. As discussed in the previous section, tube C shown to be upright on the surface in Figure 5 should show the opposite angular dependence from that of HOPG graphite. Thus, the intensity of the π^* resonance should be highest at normal incidence and lowest at glancing incidence. We report here a preliminary study of MWNTs grown onto a Pt substrate. The synthesis and characterization of these samples has been described elsewhere.[11] Parts a and b of Figure 7 show the NEXAFS spectra at glancing and normal incidence for MWNTs on Pt as well as MWNT powder, respectively.

It is apparent from the data in Figure 7b that the MWNT powder behaves almost completely isotropically. The spectra

at glancing and normal incidence look very similar. However, for the MWNT arrays grown on Pt, at normal incidence, the π^* resonance is slightly higher than the σ^* resonance, whereas at glancing incidence, the π^* resonance intensity is considerably lower than the σ^* resonance. This is, indeed, the behavior expected from a tube standing upright, as shown for tube C in Figure 5. Moreover, it is opposite to the trend noted for HOPG graphite and SWNT buckypaper. The very surface of the tube has closed caps with high curvature, which likely adds residual intensity to the π^* resonance at glancing incidence, causing deviations from the simple picture predicted by Figure 5. However, the general trend is still consistent with sample anisotropy, with tubes standing upright. We are currently investigating the anisotropy of arrays of MWNTs and SWNTs on different surfaces and will subsequently report on the use of NEXAFS in studying both MWNTs and SWNTs that are aligned vertically on surfaces.

Conclusions

NEXAFS spectroscopy is shown to be a useful probe for the investigation of order and alignment in nanotube arrays and composites. In contrast to nanotube powders, SWNT buckypaper and MWNTs arrays on Pt have been studied as model systems to investigate the angular dependence of their sidewall π^* intensities. The results are compared to that of HOPG graphite. A quantitative evaluation of order is also presented. Because several different routes including melt processing, electrospinning, metal assisted deposition and Langmuir−Blodgett techniques have been developed toward making membranes, films, fibers, forests, and other ordered nanotube systems, we believe NEXAFS will have relevance for determining the degree of order in these systems.[17,37−39] That is, orientation parameters derived from NEXAFS measurements will allow for the evaluation of relative sample anisotropy in different nanotube-based systems, which the current work establishes precedence for. Future work will also focus on detailed investigations of nanotube arrays grown on a number of different substrates.

Acknowledgment. S.B. and T.H.-B. contributed equally to this work. We acknowledge support of this work through startup funds provided by the State University of New York at Stony Brook as well as Brookhaven National Laboratory. Acknowledgment is also made to the National Science Foundation for a CAREER award (DMR-0348239) and to the donors of the Petroleum Research Fund, administered by the American Chemical Society, for support of this research. S.S.W. thanks 3M for a nontenured faculty award. Research was carried out in part at the National Synchrotron Light Source at Brookhaven National Laboratory, which is supported by the US Department of Energy under contract number DE-AC02-98CH10886.

References and Notes

(1) Dresselhaus, M. S.; Dresselhaus, G.; Avouris, P. *Carbon Nanotubes: Synthesis, Structure, Properties, and Applications*; Springer-Verlag: Berlin, 2001.

(2) Baughman, R. H.; Zakhidov, A. A.; de Heer, W. A. *Science* **2002**, *297*, 787.

(3) Avouris, P. *Acc. Chem. Res.* **2002**, *35*, 1026.

(4) Bonard, J.-M.; Kind, H.; Stockli, T.; Nilsson, L. O. *Solid. State. Electron* **2001**, *45*, 893.

(5) Bonard, J.-M.; Croci, M.; Klinke, C.; Kurt, R.; Noury, O.; Weiss, N. *Carbon* **2002**, *40*, 1715.

(6) Poulin, P.; Vigolo, B.; Launois, P. *Carbon* **2002**, *40*, 1741.

(7) Salvetat, J.-P.; Bonard, J.-M.; Thomson, N. H.; Kulik, A. J.; Forro, L.; Benoit, W.; Zuppiroli, L. *Appl. Phys. A* **1999**, *69*, 255.

(8) Dalton, A. B.; Collins, S.; Munoz, E.; Razal, J. M.; Ebron, V. H.; Ferraris, J. P.; Coleman, J. N.; Kim, B. G.; Baughman, R. H. *Nature* **2003**, *423*, 703.

(9) Fan, S.; Chapline, M. G.; Franklin, N. R.; Tombler, T. W.; Cassell, A. M.; Dai, H. *Science* **1999**, *283*, 512.

(10) Dai, H. *Acc. Chem. Res.* **2002**, *35*, 1035.

(11) Ren, Z. F.; Huang, Z. P.; Xu, J. W.; Wang, J. H.; Bush, P.; Siegal, M. P.; Provencio, P. N. *Science* **1998**, *282*, 1105.

(12) Pichot, V.; Launois, P.; Pinault, M.; Mayne-L'Hermite, M.; Reynaud, C. *Appl. Phys. Lett.* **2004**, *85*, 473.

(13) Pinault, M.; Mayne-L'Hermite, M.; Reynaud, C.; Beyssac, O.; Rouzaud, J. N.; Clinard, C. *Diamond Relat. Mater.* **2004**, *13*, 1266.

(14) Gommans, H. H.; Alldredge, J. W.; Tashiro, H.; Park, J.; Magnuson, J.; Rinzler, A. G. *Appl. Phys. Lett.* **2000**, *88*, 2509.

(15) Huang, S.; Mau, A. W. H.; Turney, T. W.; White, P. A.; Dai, L. *J. Phys. Chem. B* **2000**, *104*, 2193.

(16) Huang, S.; Dai, L.; Mau, A. *Physica B* **2002**, *323*, 333.

(17) Chattopadhyay, D.; Galeska, I.; Papadimitrakopoulos, F. *J. Am. Chem. Soc.* **2001**, *123*, 9451.

(18) Dresselhaus, M. S.; Dresselhuas, G.; Jorio, A.; Souza Filho, A. G.; Pimenta, M. A.; Saito, R. *Acc. Chem. Res.* **2002**, *35*, 1070.

(19) Kukovecz, A.; Pichler, T.; Pfeiffer, R.; Kramberger, C.; Kuzmany, H. *Phys. Chem. Chem. Phys.* **2003**, *5*, 582.

(20) Bahr, J.; Tour, J. M. *J. Mater. Chem.* **2002**, *12*, 1952.

(21) Lourie, O.; Wagner, H. D. *J. Mater. Res.* **1998**, *13*, 2418.

(22) Ichida, M.; Mizuno, S.; Kataura, H.; Achiba, Y.; Nakamura, A. *Appl. Phys. A* **2004**, *78*, 1117.

(23) Launois, P.; Marucci, A.; Vigolo, B.; Bernier, P.; Derre, A.; Poulin, P. *J. Nanosci. Nanotech.* **2001**, *1*, 125.

(24) Stöhr, J. *NEXAFS Spectroscopy*; Springer-Verlag: Berlin, 1992.

(25) Coffman, F. L.; Cao, R.; Pianetta, P. A.; Kapoor, S.; Kelly, M.; Terminello, L. J. *Appl. Phys. Lett.* **1996**, *69*, 568.

(26) Tang, Y. H.; Sham, T. K.; Hu, Y. F.; Lee, C. S.; Lee, S. T. *Chem. Phys. Lett.* **2002**, *366*, 636.

(27) Tang, Y. H.; Zhang, P.; Kim, P. S.; Sham, T. K.; Hu, Y. F.; Sun, X. H.; Wong, N. B.; Fung, M. K.; Zheng, Y. F.; Lee, C. S.; Lee, S. T. *Appl. Phys. Lett.* **2001**, *79*, 3773.

(28) Kuznetsova, A.; Popova, I.; Yates, J. T., Jr.; Bronikowski, M. J.; Huffman, C. B.; Liu, J.; Smalley, R. E.; Hwu, H. H.; Chen, J. G. *J. Am. Chem. Soc.* **2001**, *123*, 10699.

(29) (a) Banerjee, S.; Hemraj-Benny, T.; Balasubramanian, M.; Fischer, D. A.; Misewich, J. A.; Wong, S. S. *Chem. Commun.* **2004**, 772. (b) Banerjee, S.; Hemraj-Benny, T.; Balasubramanian, M.; Fischer, D. A.; Misewich, J. A.; Wong, S. S. *ChemPhysChem* **2004**, *5*, 1416.

(30) Schiessling, J.; Kjeldgaard, L.; Rohmund, F.; Falk, L. K. L.; Campbell, E. E. B.; Nordgren, J.; Bruhwiler, P. A. *J. Phys.: Condens. Matter.* **2003**, *15*, 6563.

(31) Chiou, J. W.; Yueh, C. L.; Jan, J. C.; Tsai, H. M.; Pong, W. F.; Hong, I.-H.; Klauser, R.; Tsai, M.-H.; Chang, Y. K.; Chen, Y. Y.; Wu, C. T.; Chen, K. H.; Wei, S. L.; Wen, C. Y.; Chen, L. C.; Chuang, T. J. *Appl. Phys. Lett.* **2002**, *81*, 4189.

(32) Zhou, O.; Shimoda, H.; Gao, B.; Oh, S.; Fleming, L.; Yue, G. *Acc. Chem. Res.* **2002**, *35*, 1045.

(33) Batson, P. E. *Phys. Rev. B* **1993**, *48*, 2608.

(34) Imamura, M.; Shimada, H.; Mtsubayashi, N.; Yumura, M.; Uchida, K.; Oshima, S.; Kuriki, Y.; Yoshimura, Y.; Sato, T.; Nishijima, A. *Jpn. J. Appl. Phys.* **1994**, *33*, L016.

(35) Sakai, T.; Ishikawa, K.; Takezoe, H.; Matsuie, N.; Yamamoto, Y.; Ishii, H.; Ouchi, Y.; Oji, H.; Seki, K. *J. Phys. Chem. B* **2001**, *105*, 9191.

(36) Smith, A. P.; Ade, H. *Appl. Phys. Lett.* **1996**, *69*, 3833.

(37) Casavant, M. J.; Walters, D. A.; Schmidt, J. J.; Smalley, R. E. *J. Appl. Phys.* **2003**, *93*, 2153.

(38) Guo, Y.; Wu, J.; Zhang, Y. *Chem. Phys. Lett.* **2002**, *362*, 314.

(39) Haggenmuller, R.; Gommans, H. H.; Rinzler, A. G.; Fischer, J. E.; Winey, K. I. *Chem. Phys. Lett.* **2000**, *330*, 219.